Designing gram-scale resonators for precision inertial sensors

Jonathan J. Carter,[1,2,*] Pascal Birckigt,[3] Oliver Gerberding,[4] and Sina M. Koehlenbeck[1,2]

[1] *Max Planck Institute for Gravitational Physics (Albert Einstein Institute), Callinstr. 38, Hannover, Germany*
[2] *Institute for Gravitational Physics of the Leibniz Universität Hannover, Callinstr. 38, Hannover, Germany*
[3] *Fraunhofer Institute for Applied Optics and Precision Engineering, Albert-Einstein-Str. 7, Jena, Germany*
[4] *Institut für Experimentalphysik, Universität Hamburg, Luruper Chaussee 149, Hamburg, Germany*

(Received 14 December 2023; revised 22 March 2024; accepted 25 June 2024; published 18 July 2024)

Recent advances in glass fabrication technology have allowed for the development of high-precision inertial sensors in devices weighing of the order of grams. Gram-scale inertial sensors can be used in many applications with tight space or weight requirements. A key element of these devices' performance is the behavior of a mechanical resonator. We present a detailed study on the design of resonators for such sensors. First, we consider how the mechanical parameters of a resonator couple with an inertial sensor's performance. Then, we look at how to geometrically design resonators to achieve specific mechanical behavior without undergoing brittle failure. Both analytic tools and finite element analysis are used to this end. We then derive expressions that can be used to optimize the performance of an inertial sensor for a specific sensitive bandwidth. A simple geometry used throughout the field is studied as an example. However, the results are presented in a general form so that they can be easily adapted to any required geometry and use case. Ultimately, the results presented here guide the design of gram-scale inertial sensors and will improve the performance of devices that follow them.

DOI: 10.1103/PhysRevApplied.22.014045

I. INTRODUCTION

Gram-scale, precision inertial sensors are a field seeing rapid innovation [1–8]. An inertial sensor can be defined as anything that measures an absolute force applied to a system. This measurement can be presented in a wide variety of units, and can measure in a Cartesian or rotational direction. These sensors aim to achieve a state-of-the-art performance in compact, vacuum-compatible housings. They achieve high performance through careful design to minimize noise from the thermal noise of the suspension system and interferometric readouts to measure the mechanical motion of the device precisely. Many of these sensors are designed to work alongside sensitive physics experiments, measuring and helping isolate experiments from seismic disturbances. Implementation of such sensors alongside atomic interferometers has been demonstrated [9], and there is a push to integrate such sensors in the control and isolation systems of gravitational wave detectors [8,10]. Sensors of this style are starting to make their way out of the confines of laboratories and seeing more dynamic applications, such as on spacecraft used in geodesy [11].

Inertial sensors need two parts: a means of encoding inertial motion and a means of reading out this motion. Gram-scale sensors demonstrated so far have vastly different design geometries, properties, and scopes to meet [1–8]. However, they all have some features in common. Inertial motion is encoded into the motion of a mechanical resonator. An interferometric displacement sensor reads out the motion of this resonator. The devices' small size makes them susceptible to suspension thermal noise, one of the leading noise terms in many designs [3]. A high mechanical quality factor (Q factor) mode of oscillation is needed to suppress thermal noise and demands low mechanical bulk loss materials such as fused silica and silicon [5]. The Q factor can be understood mechanically as

$$Q = 2\pi \frac{\text{energy stored}}{\text{energy dissipated per oscillation cycle}}, \quad (1)$$

effectively making it a measure of how well energy is stored in the oscillating system. Mechanical resonators of this type are usually designed with two or more thin bridges between the suspended test masses and the outer frame, which we call the flexures [1–8]. The flexures usually have a thickness of the order of 100 μm and lengths

*Contact author: Jonathan.carter@aei.mpg.de

of millimetres. These flexures can then support test masses over 1 g. Using multiple flexures, the fundamental mode of oscillation can be linear with respect to the sensing axis. Typically, the features that improve the noise performance of these resonators can also lead to brittle fracture of the thin flexures. Compromises must be made in the design to improve noise performance and survive operation and transport.

Most successful resonators in this field have been manufactured by an etching-assisted femtosecond laser ablation method first developed by Bellouard *et al.* [12] and made commercially available by FEMTOprint. The technique uses a two-step process, whereby first, any areas to be removed are "activated" by a high-energy femtosecond pulse laser. Then, the whole sample is bathed in HF acid, leaving only the desired geometry. The method allows for complex geometries to be produced [3,6]. The drawback of this method is that control of the surface roughness is not well preserved, and coating before structuring is not possible. Other methods of production are being investigated [5]. The design philosophy presented here is independent of the manufacturing method; however, as surface roughness plays a large part in the results, some estimate of residual surface roughness is needed as an example. For this, the roughness of samples produced by the FEMTOprint is tested and used. While the derived relations in this paper hold for any manufacturing method, the results will change substantially based on the resulting surface roughness.

As the field aims to make increasingly high-performance sensors, optimal design becomes critical. We present a robust approach to the design of the resonators, which are optimized for noise performance. This paper focuses on the design of the resonating part and best practices that minimize a mechanical resonator's thermal noise without suffering brittle fracture while in operation or transport. To do this, we look at loss terms in mechanical resonators and how they couple to noise performance in Sec. II. Then, in Sec. III, we study how the parameters that define a flexure geometry couple to the mechanical behavior of the resonator. Both finite element analysis (FEA) and analytical modeling are undertaken. These results are combined in Sec. IV, where the optimum choice for parameters for specific design cases is found. General equations and optimums are defined, which can be used in designing resonators for a wide range of applications. In Sec. V we then take a look at resonators used in inertial sensors in recent publications and show how, using these design techniques, better thermal noise floors could be achieved. We conclude with remarks about implementing these results into designs for inertial sensors.

II. NOISE SOURCES IN INERTIAL SENSORS

An inertial sensor can be viewed as a suspended test mass, which behaves as a simple harmonic resonator in a box. Inertial motion, X_g, the system's input, is then read out as the measurable distance from the edge of the box to the test mass, ΔX, the system's output, by the transfer function

$$\frac{\Delta X(f)}{X_g(f)} = \frac{-f^2}{f^2 - f_0^2 - if_0^2/Q}, \tag{2}$$

where f is the Fourier frequency and f_0 is the natural frequency of oscillation of the fundamental mode.

Kilogram-scale inertial sensors represent the current state of the art for precision inertial sensing across the sub-100-Hz regime [13,14]. This regime is typically the most important for sensors aiming to study seismic behavior or isolating physics experiments from seismic disturbances [9,10]. These sensors typically have kilograms of suspended mass and subhertz f_0. Gram-scale inertial sensors aim to achieve similar noise performance over the same bandwidth, but by shrinking the device's weight and size. To do so requires careful design to minimize all noise terms in the sensors.

The noise of an inertial sensor can be characterized into two groups: noise sources that disturb the position of a test mass and noises causing a measurement error of the test mass position. As gram-scale sensors typically have higher resonance frequencies than classical kilogram-scale inertial sensors [13,14], the motion of the test mass to the system input will be smaller. This mandates a precision readout method. There is much research on low-noise readout schemes that are suitable for integration with a low-noise resonator to make a complete inertial sensor [2,14–22]. As a consequence of Eq. (2), when the readout noise is white in terms of displacement, it will be white in inertial-equivalent displacement units above the f_0 of the resonator. Below its resonance frequency, inertial displacement noise will increase as $1/f^2$, and in acceleration noise, plateau at a level proportional to $1/f_0^2$. Therefore, high-performance inertial sensors commonly use a resonator with a low resonance frequency to widen the low readout noise band. One can measure below the resonance frequency of the resonator, but one suffers a penalty in noise performance for doing so, as the suspension becomes less efficient at isolating the test mass. Increasing ground motion at low frequencies and needing high-Q-factor resonators can create dynamic range issues if the inertial sensor is used as a seismometer. These factors often limit suitable readout techniques or a resonator's acceptable values of f_0.

In addition to a good readout, the mechanical oscillator must also be designed to minimize thermal noise. Without the kilogram-scale test mass, gram-scale sensors must have their mechanical resonator carefully designed to minimize noise sources that disturb the test mass position, such as suspension thermal noise. Ultimately, these noise sources are additive, so an inertial sensor will be limited

by whichever performs worse. It is therefore necessary to study how best to design the mechanical resonator to minimize coupling to thermal noise.

A. Suspension thermal noise

Suspension thermal noise is the primary source of noise that disturbs the test mass position. It originates from the thermally driven excitations of the microscopic degrees of freedom of the test mass coupling to test mass motion through the fluctuation-dissipation theorem. It is often the fundamental limit of a design. Equations defining the limits of this noise source have been well defined in several places [23,24]. Suspension thermal noise typically becomes a problem for low-frequency sensors.

How thermal noise scales depends on the damping mechanism. When the damping is related to internal flexure behavior, it usually depends on displacement. This is called structural damping. In the case of a resonator with large mode spacing between its fundamental mode and higher-order modes, the acceleration noise from structural damping is given by

$$\tilde{A}(\omega) = \sqrt{\frac{8\pi k_b T f_0^2}{mfQ}}. \tag{3}$$

If many modes are close together, a much more thorough analysis is needed [25]. However, most gram-scale inertial sensors so far aim to achieve large mode spacing between the fundamental and higher-order modes [1–8]. Typically, physics experiments wish to measure a vector of acceleration so that the correct signal can be removed from the measurement. These sensors are designed to be soft in only one direction, which means having only one mode of oscillation near the sensitive band and the others pushed to a much higher frequency. Doing so ensures that they are only sensitive to one direction of applied acceleration. In this case, the more straightforward description of acceleration noise induced by structurally damped suspension thermal noise can be described by Eq. (3). When an omnidirectional sensing solution is required, multiple sensors can be combined in an orthogonal orientation for a vector of applied linear and rotational accelerations.

The factors that make a low-noise inertial sensor are already apparent from Eq. (3). We need a high mass, low natural frequency, and high Q factor. Large inertial sensors achieve low damping losses using large proof masses with soft suspensions. Gram-scale inertial sensors must compensate for this mass loss to achieve high precision by using high Q factors, typically at least of the order of 10^4 [1,3,8].

We must therefore consider the loss terms dominant in gram-scale resonators and how to minimize them.

1. Thermoelastic damping

Thermoelastic damping (TED) has been well derived and described [26–28], and only the relevant results are stated here. It is a physical mechanism whereby, during oscillation, localized heated and cooled regions are created by expansion and contraction across the material. The energy flow from these heated to these cooled regions is an irreversible process, representing a source of energy loss from the system.

The Zener approximation can estimate TED in thin beams, which is the method used by Lifshitz and Roukes [27]. A derivation of a direct solution for the plate geometry similar to thin flexures is presented by Norris and Photiadis [28]. The key result from this is that the Q factor from TED can be approximated as

$$Q_{\mathrm{TED}}^{-1} \approx \frac{\alpha^2 E T}{C_p} \frac{\omega\tau}{1+\omega^2\tau^2}, \tag{4}$$

where α is the coefficient of thermal expansion, E is Young's modulus, ρ is the density, C_p is the volumetric heat capacity at constant pressure, and τ is the thermal relaxation time. In the case of a thin beam, this is approximated by

$$\tau = \frac{{d_{\mathrm{fwidth}}}^2}{\pi^2 \chi} \tag{5}$$

with d_{fwidth} the flexure thickness and χ the thermal diffusivity. Other geometries have been solved, but solutions become increasingly complex [28,29]. For this reason, more complex geometries often use FEA to solve the effect of thermoelastic damping [30,31].

The Q factor has an explicit dependence on the frequency. When substituted into Eq. (3), the frequency dependence cancels out at frequencies significantly below the thermal relaxation time, and thermal noise becomes flat with respect to the frequency. The second key effect from Eq. (4) is the occurrence of the TED peak in losses at a Fourier frequency of τ^{-1}. The peak can be understood physically by considering that, when the oscillation is at a frequency comparable to τ^{-1}, the heat generated from areas of the flexure that are compressed can flow to regions cooled by expansion of the material. At frequencies above τ^{-1}, the heat is less able to flow from the hot to cold regions; at frequencies below the relaxation time, smaller temperature differentials are created. We should, therefore, aim to tune this lossy peak so that it does not occur in a measurement bandwidth of interest.

2. Material, bulk, and surface loss

Another leading loss term is the intrinsic loss of the material. When studying the losses in various materials, we see that the material itself seems to have some intrinsic

loss. This loss originates from other underlying mechanisms best described phenomenologically [32]. These losses can have frequency dependence and even different values for shear and volumetric profiles. Therefore, the specific loss profiles of different materials, and even the same material from differing supplies, must be measured [33,34] to provide estimates for this loss.

Typical values for fused silica are of the order of $Q_{\text{Bulk}}^{-1} = 10^{-7}$ at room temperature [33]. The material's surface will have a less regular structure, and contaminants may be embedded in the structure, increasing mechanical loss along the surface. Typically, this is treated as having a bulk material with the material's intrinsic loss and a surface layer with a lower intrinsic loss, Q_{Surf}^{-1}, penetrating to some depth d_s. Gretarson and Harry [32] estimated a value of $Q_{\text{Surf}}^{-1} = 10^{-5}$, in the case of well-handled fused silica fibres. The value could vary wildly based on treatment, handling, and manufacturing, but it is useful as an estimate for samples kept in a clean environment. We use this interpretation to estimate a material loss term of

$$Q_{\text{Mat}}^{-1} = Q_{\text{Bulk}}^{-1} + Q_{\text{Surf}}^{-1} d_s \frac{\int_S \epsilon(\vec{r})\, dS}{\int_V \epsilon(\vec{r})\, dV}, \tag{6}$$

where ϵ is the strain energy density per unit volume. If a rough estimate is needed, one can reasonably assume that the strain energy is evenly distributed over the oscillating area or can be solved using FEA. A surface roughness measurement must be made to estimate values of d_s. Surface roughness will depend heavily on manufacturing techniques. As the production methods of FEMTOprint [12] have currently shown the best results [1,8], we take measurements on samples produced in this manner and use those as the estimates for the discussion in Sec. IV.

Fused silica is a standard choice for a room-temperature high-Q resonator [1]. Fused silica is used due to its low bulk loss and comparatively high shear stress to other low-loss glasses [33]. Numata *et al.* [33] studied the specific bulk losses for several types of fused silica; good candidates for specific materials were Corning 7890-0F and Heraeus Suprasil-312. The latter has a slightly lower bulk loss, but both make excellent candidates. Corning 7890-0F is used in the design example cases in Sec. IV as it is a material the authors have used to make high-Q-factor resonators.

The roughness of samples produced by FEMTOprint was measured. The surface roughness was studied using a laser scanning microscope. The first region studied was where removed material left a surface which was parallel to the laser's angle of incidence. These surfaces were needed for the resonator of this geometry. Samples with differing geometries have been produced in previous works [3]. These samples had a laser incident on the normal of the surface, and so we can compare the two different angles of attack. The definition of the way the laser is incident on the resulting surface is shown in Fig. 1. The profiles and the average value taken were measured over nine lines in a hashed pattern. Ultimately, the parallel incidence side had an R_z (the mean peak-valley distance of five chunks of the sample region) of 7.0 ± 1.0 μm, but an R_z of 10.0 ± 0.7 μm was measured for the normal incidence beam, which is used as an estimate of d_s for the rest of this work. A cut-off wavelength of $\lambda_c = 0.8$ mm was used for both these estimates. The samples represent the average values from nine segments drawn in a hashed pattern over the surface. The lines were 0.25 mm long and had a spatial resolution of 130 nm.

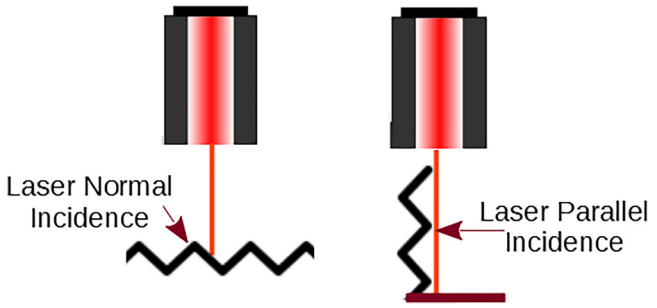

FIG. 1. The two possible angles of attack for a laser with respect to the remaining flexure surface. Both types of incidence were assessed for the resulting surface roughness.

III. DESIGN OF LOW-NOISE MECHANICAL RESONATORS

The flexure's behavior is defined by its geometry, much more than the overall geometry of the resonator. Therefore, we wish to use a simplified geometry to study good flexural design techniques. Well-designed flexures can then be fit into an overall geometry based on the use case. We consider a simple parallelogram linear geometry, as shown in Fig. 2. The parameters shown in Fig. 2 are studied throughout this section to show their effects on the resonator. The optimum flexure parameters are discussed in Sec. IV.

Such geometries have been produced as sensors in several applications [1,4,8,35]. The parallelogram structure forces the fundamental mode into a linear in-plane motion, as shown in Fig. 3, which makes reconstructing inertial motion from measured test mass motion possible with simple transfer functions. So far, most of these structures have worked with the maximum of any dimensions below 10 cm, with suspended masses of several grams shown. The flexures have a d_{fwidth} of the order of 100 μm, while d_{flength} has been shown up to 7 cm [8].

The key elements we study are how to tune the frequency of the fundamental mode, make the resonators survive in their intended operational environment, and combine these to optimize a design's thermal noise.

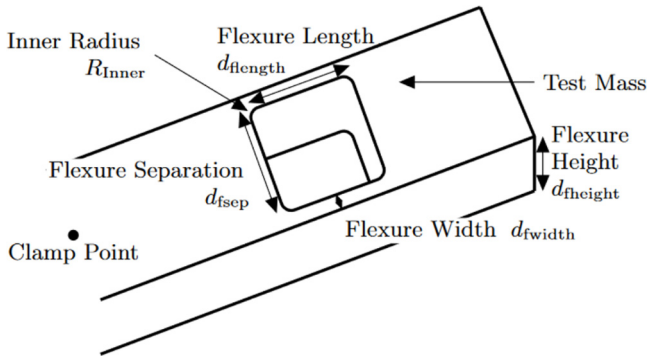

FIG. 2. Geometric definitions of the terms discussed in the flexure design. Although the overall geometry of the device may change, the definitions of the flexure length, separation, width, and height stay the same. In this case one flexure junction is shown, in others, multiple flexure junctions may be used. The test mass is the suspended mass that is not rigidly attached to the ground; it is always on the opposite side of the flexure junction to the clamping point. The clamp point is the point (or interface) at which the monolithic piece is rigidly attached to the ground.

A. Tuning resonator resonances

The most critical parameter in the design of an inertial sensor's resonator is its fundamental resonance frequency, f_0. The resonance frequency f_0 defines how the system responds to external forces, determines what readout methods are appropriate both with respect to the dynamic range and noise performance, and contributes to the thermal noise limitations.

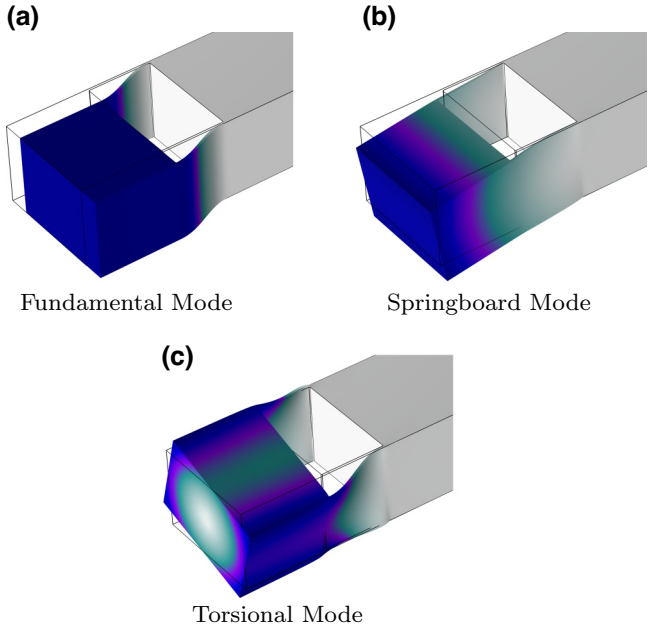

FIG. 3. The first three eigenmodes for a linear parallelogram resonator. (a) The fundamental mode is linear regarding excitations from the side, which can be used to track inertial motion. (b) The springboard motion acts up-down, perpendicular to the direction of fundamental oscillation, but acts as an additional energy loss from the system. (c) The torsional mode will couple directly to measurements of the test mass displacement and so must be suppressed using design. The heat map shows the local displacement at the extrema of the oscillation with arbitrary scaling.

Along with achieving a target f_0, we wish to tune other modes so that there is a significant frequency gap between them and f_0 and the target sensitive bandwidth. Various problematic effects can occur when these modes are too close, such as phonon-phonon loss [36], beam pointing issues in optical readout schemes, and nonlinear effective motion at the point used for displacement sensing. Figure 3 shows the shape of the first three oscillation modes for a linear resonator.

In order to study tuning of mode frequencies, the COMSOL Multiphysics® FEA software was used. The PARDISO solver was used to calculate solutions. For most simple geometries, the solution converged to a relative tolerance between iterations of 10^{-16} after ten iterations. Some more complex geometries required closer to 100 iterations to achieve this level of convergence. If the study was not converging, a finer mesh size was used.

A linear resonator was studied with the parameters shown in the last panel of Fig. 4. For each graph, one parameter is varied while keeping the other four parameters constant. When not studied, they took the values shown in the last panel. The effect on each of the three fundamental modes is shown in the relevant plot.

From Fig. 4 we can now show the fundamental mode evolves with respect to the geometric parameters as

$$f_0 \propto \sqrt{\frac{{d_{\text{fwidth}}}^3 d_{\text{fheight}}}{{d_{\text{flength}}}^3 m(d_{\text{flength}}, d_{\text{fheight}}, d_{\text{fsep}})}} \tag{7}$$

with m a function of the geometric variables of the oscillator. Geometries such as a linear oscillator have an independent means of tuning m with the length of the test mass, but other geometries such as a drum geometry [3,6] do not. We consider the case in which m can be independently tuned, but any following equation can be adapted for the case in which it cannot by substituting the relevant evolution of m with respect to the geometric parameters.

Parameters that add stiffness in the direction of the oscillation cause the frequency of that mode to increase by a power of 3/2, while adding general stiffness or mass increases it by a power of 1/2.

The other modes do not evolve as standard power laws. Many follow peak-shaped relations as different effects take over and dominate the response. In general, we see that increasing d_{fheight} best optimizes the gap between modes, while lower-frequency fundamental modes can be achieved both by the reduction of d_{fwidth} or d_{flength}.

A problem one must be aware of is the internal modes in the flexures themselves. When too thin or long, the test mass and clamp side act as anchors and the system

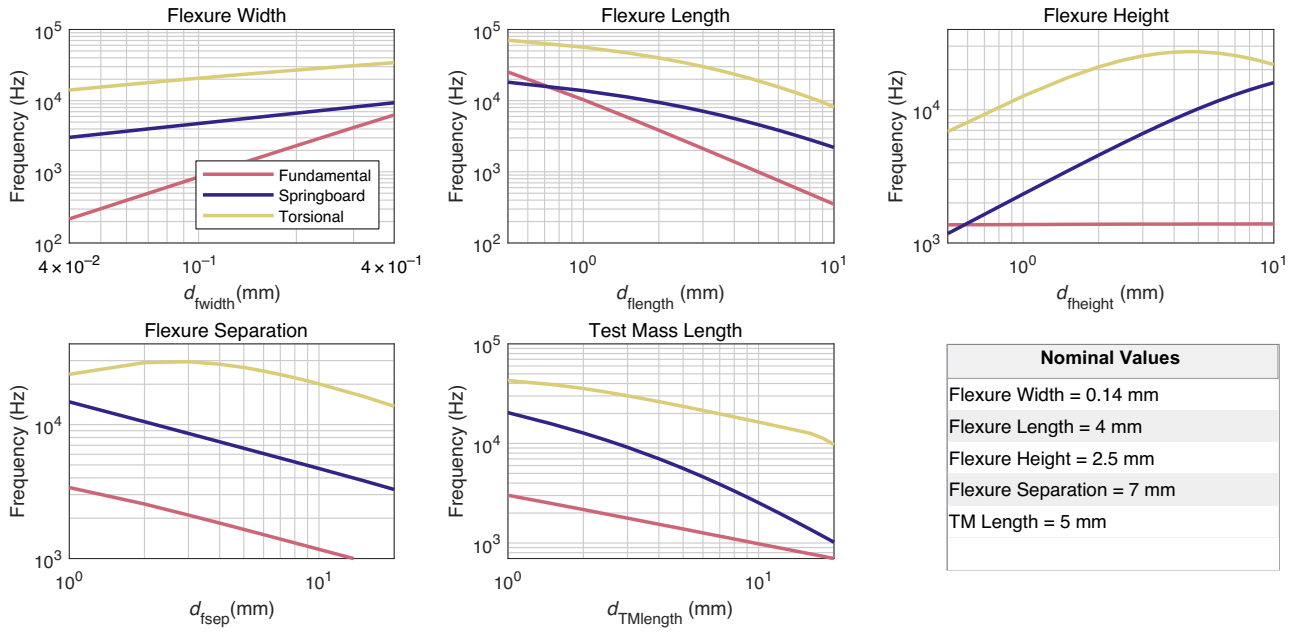

FIG. 4. Graphs showing how the eigenfrequencies of a linear parallelogram resonator's first three modes of oscillation vary with changing parameters from Fig. 2. The table of nominal values shows the parameter's value when it is not under investigation. The eigenfrequencies were predicted using the COMSOL Multiphysics FEA software. For geometric reasons, the mass increases linearly when the height or separation increases. Most resonators aim to achieve the maximum possible separation between the higher-order and fundamental modes. This figure can be used to estimate the response of the resonator's mode frequencies to parameter changes and can be used as a guide to achieve the desired resonator behavior.

becomes akin to a system where a thin beam is clamped on both ends. This behavior is especially problematic as the motion of the fundamental mode will directly couple to these modes and lead to a significant dissipation of energy from the system.

Furthermore, one must be careful of nonlinear effects from higher-order modes coupling to the fundamental mode. The angle of the torsional mode, for example, would lead to tilt-to-length coupling [37] in the readout. The scale of this effect will depend on the specifics of the readout method and how well the readout is centered on the test mass. Ultimately, the effect will lead to a limitation on the dynamic range, as the measured motion will be dependent on the input forces to the sensors. In cases where the precision readout is required in a noisy environment, this effect must be fully studied. To minimize this effect, a large frequency difference between the fundamental and higher-order modes must be achieved, but this limit will depend on the use environment. In the specific case that the motion of the environment studied is very low, we would like to tune these frequencies such that f_0 is at its correct target, based on the readout method and noise requirements, while f_1 is above the target measurement bandwidth.

Our FE analysis shows that the fundamental mode of oscillation can be separated from the springboard and torsional modes with a large flexure height and separation. Low-frequency oscillation of the fundamental mode can be achieved by increasing the flexure length and decreasing the width. It should also be noted that calculations based on the thermal noise of the device derived throughout the paper are only valid when a large mode separation has been achieved.

B. Resonator survival

From Sec. II, a need for low-frequency oscillations has been demonstrated. If the material is fixed in choice, this only leaves geometric considerations, but changing the parameters can make the samples more prone to brittle fracture. We must therefore study how best to prevent brittle fracture in the resonators and how to make them survive their expected environmental conditions.

A simple failure model can be used if motion and stress are confined or largely dominated by one direction. In this case, the stress induced by a given load can be simulated using FEA. Points in the geometry of high stress can be compared to the failure condition. The maximum shear stress criterion can be used to predict failure in resonators undergoing parallel motion, where most stress is confined to the direction of travel. We can then define a safety factor for all points in the sample

$$\frac{F_U}{\sigma} = \text{safety factor}, \tag{8}$$

where F_U is the ultimate shear strength and σ is the shear stress at the given point in the resonator. A safety factor of less than 1 indicates that the material will fail at that point; however, it is advisable to always leave some margin of error for extra unexpected loads. Furthermore, ultimate failure points in glass typically have large uncertainties as they strongly depend on local structure defects and contaminants.

The highest load a resonator can expect to face depends on its environment. For many sensors used in a terrestrial environment in controlled laboratory space, the maximum stress induced is when gravity acts in the direction of oscillation and is free to fall. For this reason, along with the relatively high cost of making a sample, a safety factor of at least five whilst under 1 g of load was used as a minimum baseline here.

FEA can be used to estimate the stresses across the material while under various loads. Again, COMSOL Multiphysics was used to solve the stress distribution. The solid mechanics and heat transfer packages in COMSOL Multiphysics were used to study the stress effects under prescribed test mass displacements. The displacement of a resonator under load from gravity is defined by

$$d_{\text{sag}} = \frac{g}{\omega_0^2}, \tag{9}$$

so the displacement a resonator must survive under depends on the resonance frequency.

Several parameters can be tuned to increase the survivability of the resonators. One that may at first seem counterintuitive is decreasing the flexure width. Naturally, one thinks of making the support thicker, and while this would lower the stress, it also increases the natural frequency. If one increases the test mass to compensate for this, the displacement remains the same, so the flexure must bend the same while being stiffer, increasing material stress. Therefore, thinning the flexure and supporting less weight will increase survivability. Practical considerations limit how thin the flexures can be manufactured, so we must look to other terms to improve survivability. Figure 5(a) shows the effects of the flexure width on maximal beam stress.

Alternatively, the flexure length can be increased. Doing so reduces the curvature per unit length and the stresses induced. Figure 5(b) shows the result of varying the beam's length; we can see the point at which a safety factor of five is reached. The figure estimates the flexure geometry required for a specific f_0. A clear indication here is that, in this regime, the d_{flength} requirement increases inversely proportional to f_0. Hence, from the simulations in Fig. 5, we can extract power-law relations between different parameters on the maximum stress in the flexures, σ_{Max}. under a

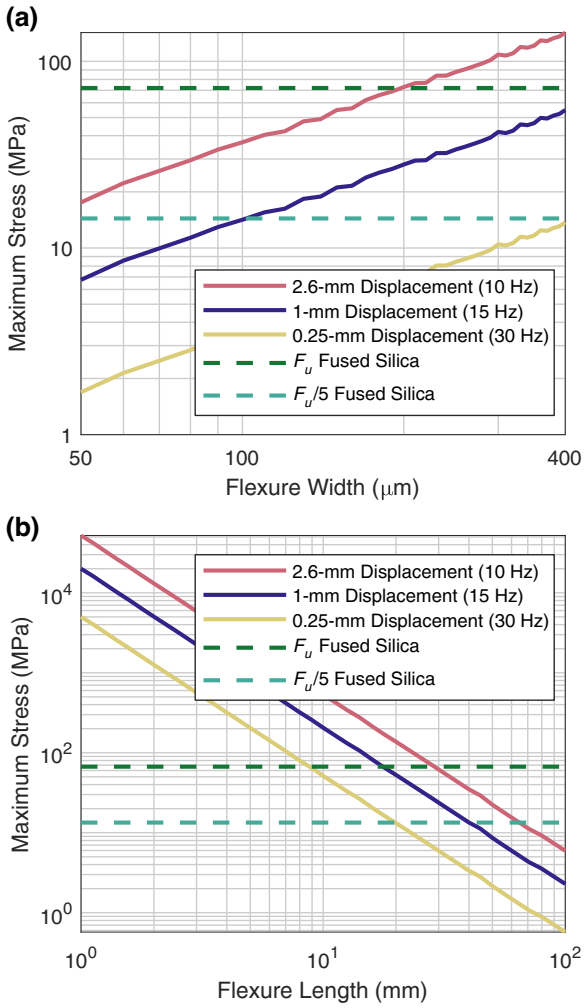

FIG. 5. The point of maximal stress in a fused silica beam with $d_{\text{fheight}} = 8$ mm when undergoing flexural motion in the direction of the width, as a function of beam width (a) and length (b). When not being studied, the length is held at 40 mm and the width at 100 μm. The stress was simulated using COMSOL Multiphysics. The solid lines correspond to different fixed displacements, which correspond to the sag related to a resonator of different fundamental frequencies under 1-g load, shown in brackets. The frequencies are chosen to span a range relevant to precision inertial sensors. The dashed lines correspond to the ultimate shear strength of fused silica, F_u, and this divided by five; any resonator under this line has a safety factor of five when tilted against gravity.

defined load, σ_{Max} evolves as

$$\sigma_{\text{Max}} \propto \frac{d_{\text{fwidth}}}{{d_{\text{flength}}}^2 f_0^2}. \tag{10}$$

This result agrees with the behavior of the analytically solved Timoshenko-Ehrenfest beam theory [38], which describes beams free on one end.

The other parameter that can be tuned for optimal stress is the inner radii of the corners of the resonator. The gains from inner radii are limited, but are studied in Appendix A.

We find that to improve the survival of the oscillator against brittle fracture, the flexure thickness must be decreased and the length increased.

C. Strain distribution in flexural motion

Equation (6) shows how we need to understand the strain energy distribution through the flexure to estimate the Q factor properly.

The theoretical strain energy distribution was solved for an ideal, infinite plate with fixed edges by Norris [28]. As the flexures on these resonators are considerably taller than they are wide, only the edge effects need be considered differently, but as the stress vectors have no component in the direction of height during oscillation, these effects are minimal. At the point of maximum displacement during oscillation, all energy should be potential energy. The strain energy distribution is given by

$$\mathcal{E}_{\mathrm{PE}} = \frac{{d_{\mathrm{fheight}}}^4}{24}\frac{1}{1-\nu^2}(E\kappa_{yy}^2), \tag{11}$$

where κ_{yy} is the element of the curvature tensor with respect to the direction parallel to the flexure length. Except for edge effects, the strain depends only on edge curvature and is uniform across the width and height. Therefore, we only consider effects across the flexure length. If the flexure is homogenous across its length, the distribution can be estimated as uniform. The flexures can be designed so that they are not homogenous along their length. We explore this in Appendix A.

IV. MINIMIZING THERMAL NOISE THROUGH FLEXURE DESIGN

We now use the information discussed so far to optimize the design parameters of the flexures in an inertial sensor. We consider two cases.

A. Free design

In the first case, we give an entirely free design space and aim to find the optimal design with respect to thermal noise. We assume that the sensor is operated in an environment such as a vacuum, so that viscous damping is irrelevant, and that the sensor aims to survive a defined load. We must consider Eq. (3) to optimize structural damping. Each term in this equation is defined by the flexure parameters defined in Fig. 2. The effects of each parameter were calculated and described in Sec. III, and so the resonance frequency is related to the geometric factors by Eq. (7). Meanwhile, Eq. (10) shows that the maximum stress in the flexure scales with the length and thickness. Combining these, the maximum possible mass for a given stress will evolve as

$$m \propto \frac{{d_{\mathrm{fwidth}}}^2 \sigma_{\mathrm{Max}} d_{\mathrm{fheight}}}{d_{\mathrm{flength}}}. \tag{12}$$

Substituting this into Eq. (3), we find that the acceleration thermal noise scales as

$$\tilde{A}_{\mathrm{TN}} \propto \sqrt{\frac{T}{d_{\mathrm{flength}} Q(d_{\mathrm{fwidth}}) d_{\mathrm{fwidth}} {\sigma_{\mathrm{Max}}}^2}}. \tag{13}$$

The ideal flexure width depends upon the target Fourier frequency in relation to the TED peak and its magnitude with respect to surface losses. The evolution of the Q factor with respect to d_{fwidth} is

$$Q = \mathrm{const} \quad \text{(bulk loss limited)}, \tag{14}$$

$$Q \propto d_{\mathrm{fwidth}} \quad \text{(surface loss limited)}, \tag{15}$$

$$Q \propto \frac{1}{{d_{\mathrm{fwidth}}}^2} \quad \text{[TED limited (below peak)]}, \tag{16}$$

$$Q \propto {d_{\mathrm{fwidth}}}^2 \quad \text{[TED limited (above peak)]}. \tag{17}$$

These responses create two scenarios. The flexures should be tuned to be as thick as possible when above the TED peak. Below the TED peak, they should be tuned such that the term

$$\frac{1}{d_{\mathrm{fwidth}}}\left(d_s Q_{\mathrm{Surf}}^{-1}\frac{\int_S \epsilon(\vec{r})\,dS}{\int_V \epsilon(\vec{r})\,dV} + Q_{\mathrm{Bulk}}^{-1} + \frac{2\alpha^2 ET}{C_p \pi \chi} f d_{\mathrm{fwidth}}^2\right), \tag{18}$$

is minimized across the desired frequency range, where we have taken the equations for Q_{Mat} and Q_{TED} from Sec. II. Typically, for precision inertial sensors for seismic measurement a bandwidth of 0.1–100 Hz is relevant. The flexures must be centimeters thick for low-frequency seismic isolation to push the TED peak below this band. Such thick flexures are not a feasible design strategy with current manufacturing techniques and go into ranges where assumptions we have made break down. Hence, we should focus on tuning the peak frequency to above detection bands. We consider how best to do this for a single flexure in Figure 6. We can use this graph to choose a flexure width for a sensor targeting a specific bandwidth. However, if we desire sensitivity over a larger bandwidth, we have to be more careful and look across the relevant frequency region. In this case, it is better to look at the effect of the flexure width on Eq. (18), across the whole bandwidth. Figure 7 shows this for four different flexure widths. Although a thicker flexure improves the thermal noise floor, it does come at the cost of high-frequency performance. There are a few ways of deciding on the flexure width from this

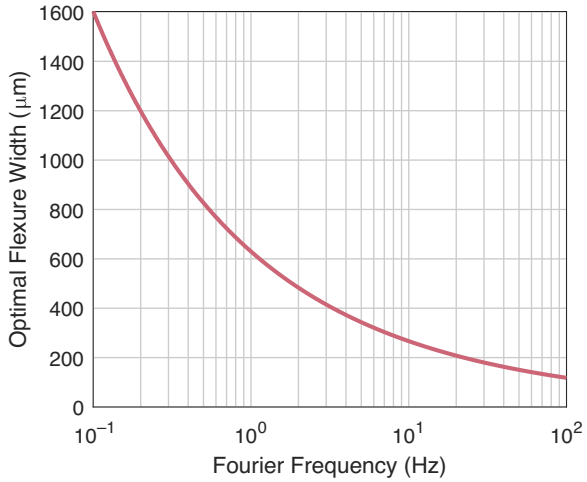

FIG. 6. The flexure widths needed to achieve minimum thermal noise at a specific Fourier frequency. Here, Eq. (18) was minimized for the flexure width as a function of Fourier frequency, and the value was plotted. For this figure, the approximation that the strain density is uniformly distributed over the flexure width is made (see Appendix A), a material of Corning 7890-0F fused silica is used, with a surface loss of 1×10^{-5} [32], with a surface depth of 10 μm from measurements in Sec. II A 2.

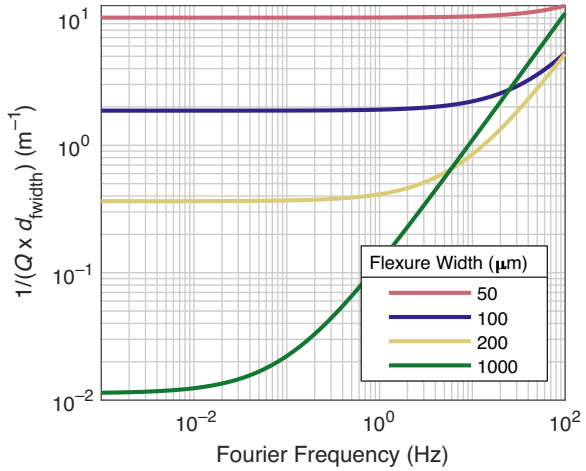

FIG. 7. The results of term (18) for flexures of four different widths across the Fourier frequency range of interest to the seismic isolation community. The strange units are effectively a proxy for thermal noise. The same assumptions, values, and material used in Fig. 6 are used here.

figure. A maximum acceptable noise floor across all frequencies could be targeted (particularly if readout noise is already known), and a flexure width that does not violate this at any frequency chosen. Alternatively, some (possibly weighted) average taken over the desired range could be used as a minimization criterion. Often, this decision is also defined by what can be made. Ultimately, the optimum flexure width is a very project-specific definition. Expression (18) can be used to find a d_{fwidth} that meets these conditions for any targeted performance

With two caveats, the flexure length should be tuned as long as possible. Lengthening the flexures is the most difficult parameter change to achieve with current manufacturing methods in terms of cost and complexity. Even if this can be achieved, there are still fundamental limits to how far the flexure length can be taken. As the flexures get longer, the test mass gets smaller. Eventually, a point will be reached where internal flexure eigenmodes are significantly induced, disturbing the test mass position.

The flexure height and separation must be tuned to give the correct f_0 and m from Eqs. (7) and (12). Ultimately, this will lead to lower heights and masses with softer springs and lower f_0 winning out in terms of thermal noise. Factors such as the radii of curvatures are discussed in Appendix A, but already have fixed optimums without the need for trade-offs. A study following the steps discussed can find these points for any flexure, and the only reasons not to include them are for manufacturing simplicity.

B. Resonance frequency fixed

Often, limits on the readout and application define f_0. With f_0 defined, the question is how to optimize around this restriction for thermal noise. Again, we can consider the same factors as in Sec. IV A, but now with the additional criteria that f_0 is constant. The limitation places a restriction

$$d_{\text{flength}} \propto \frac{d_{\text{fwidth}} d_{\text{height}}{}^{1/3}}{m^{1/3}} \tag{19}$$

in order to maintain the correct resonance frequency. The restriction also applies to the maximum suspendible test mass

$$m \propto \sigma_{\text{Max}}{}^{3/2} d_{\text{fwidth}}{}^{3/2} d_{\text{height}}. \tag{20}$$

With the resonance frequency fixed, thermal noise is controlled by the mQ product. Substituting limitations into Eq. (3), we get the scaling

$$\tilde{A}_{\text{TN}} \propto \sqrt{\frac{T}{d_{\text{fheight}} Q(d_{\text{fwidth}}) d_{\text{fwidth}}{}^{3/2} \sigma_{\text{Max}}{}^{3/2}}}. \tag{21}$$

The condition on the width is slightly adapted from the free design case

$$\frac{1}{d_{\text{fwidth}}{}^{3/2}} \left(d_s Q_{\text{Surf}}^{-1} \frac{\int_S \epsilon(\vec{r})\, dS}{\int_V \epsilon(\vec{r})\, dV} + Q_{\text{Bulk}}^{-1} + \frac{2\alpha^2 ET}{C_p \pi \chi} f d_{\text{fwidth}}^2 \right), \tag{22}$$

which must again be minimized with equivalent graphs to Figs. 6 and 7. This again leads us to a similar optimization study as in Sec. IV A for the flexure width.

A key difference here is the scaling with flexure height. Increasing the flexure height allows a greater mass to be suspended, making the flexures stiffer. This scaling will allow for a heavier test mass without compromising maximal stress. The limits here are again similar to the length scaling in the previous case. The increased height will lead to a larger volume etched, increasing the manufacturing cost and complexity of the devices. Furthermore, Fig. 4 shows that the torsional mode will eventually become problematic as the height is increased. The length of the flexures is defined by what is needed to survive under load. The supported mass can then be tuned to give the correct f_0.

C. Practical design of gram-scale resonators

We have now evaluated the tools we have at our disposal to geometrically design gram-scale resonators for inertial sensors. With this, a general method of sensor design can be reached.

The first step is to define the sensor requirements and limitations. If specific readouts and noise performance are needed, f_0 can often be fixed. If the sensor is intended to operate in a noisy environment, a greater mode spacing between the fundamental and higher-order modes is needed and a study on the required spacing would be needed. Furthermore, understanding its use environments determines the maximum load that a sensor needs to be able to survive.

From here, specific geometric parameters can be tuned to achieve the desired performance. These can be done in the following order.

(a) The flexure thickness d_{fwidth} can be optimized with results from Eqs. (18) and (22). Depending on the geometry, this can be mapped onto whichever parameter sets the stiffness in the desired oscillation direction.

(b) The d_{flength} or other relevant survivability criteria can then be set to survive under the expected load.

(c) The d_{fheight} and m along with any other f_0 tuning parameters can give the required f_0.

(d) The overall geometry can then be tuned to meet the required oscillation mode separation.

With these scalings and manufacturing techniques, a "bang-for-your-buck" approach is reached, whereby even when optimized, there is a scaling financial cost to reaching a specific noise performance. Usually, the best approach is to estimate the noise floor from the readout and design the resonator to achieve high enough performance that the thermal noise no longer dominates at the relevant frequencies.

When an ideal resonator is designed, tolerances on design parameters should be considered. The relevant tolerances will be subject to both manufacturing methods and overall geometry. Appendix B discusses the specific case of resonators produced through subtractive manufacturing methods, such as those presented by Bellouard *et al.* [12].

V. APPLIED RESONATOR DESIGN

We now have a means of optimizing the resonator design. Still, we wish to demonstrate its effectiveness by re-evaluating a resonator shown in a recent publication and showing how the design could be altered to lower the thermal noise floor of the resonator. The first resonator considered is that used in a recent publication by Hines *et al.* [8]. They discussed a full inertial sensor that achieves excellent noise performance at a subhertz regime with the use of a similar geometry as studied here. The sensor shown in [8] had an f_0 of 5 Hz, and a measured Q factor of 477 000 on resonance. The flexures of this piece had $d_{\text{flength}} = 70$ mm, $d_{\text{fheight}} = 6.6$ mm, $d_{\text{fwidth}} = 100$ μm, and a test mass of 2.6 g. These samples were also produced by FEMTOprint. The authors stated that they expected a Q factor of 4 000 000, but this only considers the intrinsic loss of bulk-fused silica. We can re-evaluate the estimate when we look at the estimates of the Q factor discussed in Sec. II. The sample was etched with a parallel incidence laser, as shown in Fig. 1, but the larger faces on both sides of the flexures were etched. Using the measured estimate of surface roughness from Sec. II A 2 of 7 μm on both large faces of the flexure and the equation for Q factor on resonance,

$$Q^{-1}(f_0) = Q^{-1}_{\text{Mat}} + Q^{-1}_{\text{TED}(f_0)} = \left(d_s Q^{-1}_{\text{Surf}} \frac{\int_S \epsilon(\vec{r}) dS}{\int_V \epsilon(\vec{r}) dV} + Q^{-1}_{\text{Bulk}} + \frac{2\alpha^2 ET}{C_p \pi \chi} f_0 d^2_{\text{fwidth}}\right). \tag{23}$$

We can estimate a value of Q^{-1}_{Surf} for this sample of 1.2×10^{-5}, which, considering the uncertainties on surface roughness, agrees very well with the estimates from Gretarsson [32], giving good validation of our model.

In order to make a fair comparison to the current design, we attempt to constrain ourselves to the same design requirements as those of Hines *et al.* [8]. In this case, we aim for the same resonance frequency, the same minimum safety factor under load, and the same d_{fheight}. The height d_{fheight} is fixed, as it is largely at the maximum dimension that can be etched in this direction with current techniques. From our discussion in Sec. IV B, increasing d_{fheight} directly improves resonator performance, and so the only reason not to push this higher is manufacturability. We assume that the same geometry is desired, and in this case do not add a radius of curvature as discussed in the appendices.

The design in question uses a motion stop at 8-mm distance from the test mass rest position. A motion stop effectively fixes f_0 in Eq. (10), at a value that is independent of the actual f_0. When resting on the motion stops, FEA

predicts that the design has a safety factor of 2. However, as our expressions mainly rely on proportionality, we can use all of the analysis in Sec. IV B.

With d_{fheight} fixed, the problem collapses down to a problem with effectively one free variable, d_{fwidth}, as m and d_{flength} must be tuned to meet requirements on f_0 and σ_{MAX}, respectively. The test mass (TM) length and d_{fsep} are semifree parameters to tune the torsional mode and springboard frequencies while maintaining the targeted test mass. The long flexures mean that we would want very high flexure separations. In practice, these large separations would massively increase the manufacturing cost of the devices, so we would rather tune the higher-order modes outside our bandwidth of interest. The designs presented in Ref. [8] aim to be used in a gravitational wave detector's active control scheme. Hence, they aim to operate well across the whole relevant control bandwidth of a gravitational wave detector [39,40]. This band is typically across a low-frequency range of 0.03–100 Hz. We therefore look for the sensors that perform best in this band.

Defining how we evaluate "optimal" performance will drastically change the result of our analysis. We therefore consider different targets to optimize and evaluate each of their effects. The first definition we consider is to minimize the noise at the high end of the sensitive frequency band of the sensor. Using Eq. (22), we optimize the resonator at the highest part of the frequency band, 100 Hz. The result was a resonator with $d_{\text{fwidth}} = 138\ \mu\text{m}$, with a corresponding increase in $d_{\text{flength}} = 82$ mm and $m = 4.6$ g. The result of these changes on the theoretical noise floor is shown in Fig. 8. This criterion shows a slight improvement at the high end of the frequency band, but a broadband improvement is seen at lower frequencies by a factor of 3/2. Already, using this simple criterion, we see a means of optimizing the design for its target sensitive band. FEA analysis on the new design validates that we meet the same design specifications of 5 Hz f_0 and a safety factor of 2 when resting on the motion stop.

The first design is optimized effectively for the high frequency, but we also wish to consider other possibilities. When we aim to optimize the sensitive band's lowest frequency, 30 mHz. Doing so gives $d_{\text{fwidth}} = 3$ mm, with a corresponding $m = 400$ g, and $d_{\text{flength}} = 5$ m. The absurd proportions of the device effectively indicate an unbounded problem in the design. Because the TED loss is also very low at these low frequencies, nothing is constraining the increasing flexure width to push down surface losses and increasing m, which results in the approach to an extrema. This tells us that improving low-frequency performance becomes an issue of manufacturing larger pieces rather than design. If one seeks performance at such low frequency, the best approach would be to lift the limit on f_0 and allow for a lower-frequency resonator.

If instead of the best performance at a specific frequency being targeted, a target over a broader band is needed, we

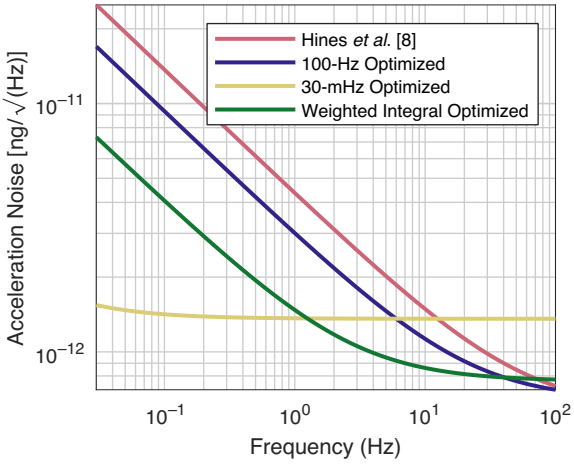

FIG. 8. The figure shows the suspension thermal noise floor in the acceleration spectral density for three different designs of the work in Ref. [8]. The red line shows the original design's noise floor. The blue, yellow, and green lines show resonators that still meet the original design specifications, but use the method presented here to optimize their thermal noise floor. The blue line shows when the performance is optimized for 100 Hz, the yellow when the performance is optimized for 30 mHz, and green when an integral over the frequency range 0.03–100 Hz is used, weighted by a $1/f$ term.

can get more nuanced with our choice of what to optimize. A naive approach would be integrating Eq. (18) over the whole bandwidth. However, doing so will result in a similar result to choosing a single high frequency, as higher frequencies will have a much larger weight on the overall integral. Instead, we can weigh the integral by a $1/f$ factor to better represent the whole bandwidth. This resulted in a resonator with $d_{\text{fwidth}} = 287\ \mu\text{m}$, with a corresponding $d_{\text{flength}} = 120$ mm and $m = 12.6$ g. Again, FEA validated that this new resonator did not violate any of our requirements on f_0 or the safety factor. The green line in Fig. 8 shows the acceleration noise floor of this design. This line is lower than the original design across most of the relevant bandwidth by a factor of approximately 3. The cost of this is a small sacrifice in performance at the high-frequency end of the bandwidth.

The method of producing resonators described here was used in another recent publication to design a 50-Hz resonator [41]. The paper used this process to produce resonators that achieved excellent thermal noise performance and also matched the estimates of the behavior on the Q factor.

VI. CONCLUSIONS

We have thoroughly explored the design of mechanical resonators for use in gram-scale precision inertial sensors. A simple geometry has been used to study the effects of various design parameters on the resonator's behavior.

From this behavior, optimal flexure parameters have been shown, for example, in design cases. The simple geometry and method here are easily adapted for more complex geometries. Example resonators have been designed that show how, using this method, resonators with optimal noise floors can be produced that outperform the best-shown resonators to data in broad frequency bands. The guides and results presented here are a base for designing such resonators for a wide range of applications.

A clear target bandwidth and sensitivity should be the starting point when designing such resonators. We can define an optimum flexure width, leading to the required length. The flexure height and test mass can be tuned for specific resonance frequencies and thermal noise floors. Understanding how these parameters interact takes a complicated interlinked multivariable problem and reduces it to a series of linear optimal point studies. Following this approach will lead to better resonator designs.

Ultimately, better resonator designs will lead to better inertial sensors. These, in turn, offer an effective solution to the many experiments seeking to isolate residual disturbances from seismic motion. With this, we will be better able to answer many fundamental physical questions still open today. As the technology of gram-scale inertial sensors progresses, it will move outside the confines of specialized physics laboratories and into general public use and consumer production. From here, the potential applications of the technology are wide open.

ACKNOWLEDGMENTS

The authors would like to acknowledge advice and support from Gerhard Heinzel, Benno Willke, and Harald Lück, and insightful discussions with Felipe Guzman.

J.J.C., P.B., and S.M.K. acknowledge funding in the framework of the Max-Planck-Fraunhofer Kooperationsprojekt "Glass Technologies for the Einstein Telescope (GT4ET)."

O.G. was funded by the Deutsche Forschungsgemeinschaft (DFG, German Research Foundation) under Germany's Excellence Strategy – EXC 2121 "Quantum Universe" – 390833306.

APPENDIX A: OPTIMAL RADII OF CURVATURES

The effects of the inner radius on the stress distribution were studied by using FEA simulation in COMSOL. The geometry shown in Fig. 9 was used for this test. A single flexure was tested, where a prescribed displacement of 25 μm was applied to one end and the other fixed in place, with no motion. The flexure was 1 mm long and had a minimum width and height of 100 μm. Then, the maximum stress along the flexures for different radii of curvatures was compared.

Figure 10 shows the results of this simulation. A radius of curvature was applied in two directions. When the radius of curvature was applied to the height, it was found that a larger radius distributes the stress better over the surface. Therefore, creating an hourglass reduces the maximum stress sustained in the flexure. Changing the width along the length of the flexure creates a minimum stress with a relatively small radius of curvature, which then increases again. Both these results have a simple physical interpretation. The width response results from a better stress distribution conflicting with thicker parts having to bend more. There is no effect of more material bending from an extra height radius of curvature, so we only see the gains from better distribution. The small rise in stress as the flexure inner radius approaches half the flexure length is likely

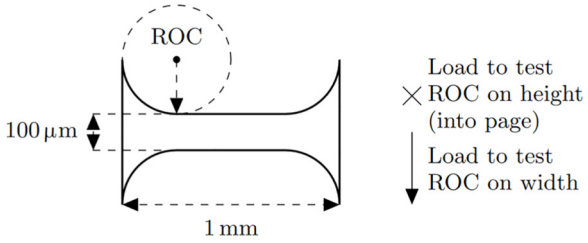

FIG. 9. A diagram showing the flexure geometry used for the radius of curvature (ROC) test. The design is 100 μm deep into the page. A load can be applied normal to the geometry to study the effects of the flexure height. To simulate a radius of curvature in the width, the load can be applied downwards, as shown by the arrow.

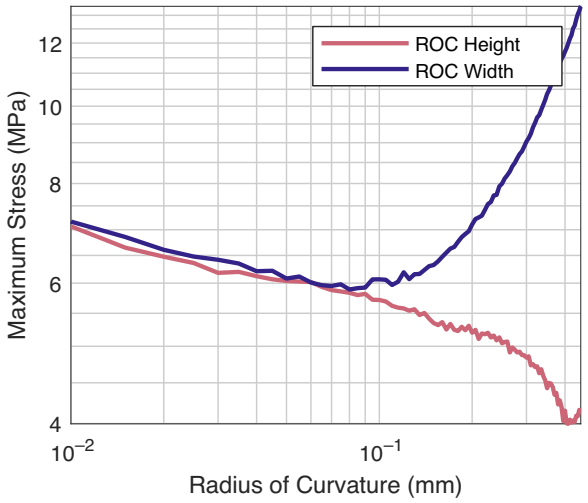

FIG. 10. The ROC versus the maximal stress in a 1-mm-long sample undergoing flexural motion with a maximal end displacement of 25 μm. The radius of curvature was applied in one of two directions: one in the direction of the flexure width and one in the direction of the flexure height. The minimum flexure width and height were 100 μm when the curvature was applied in that direction. When the curvature was not applied in that direction, they were flat at 100 μm. The simulation used COMSOL's stationary solver with its solid mechanics module.

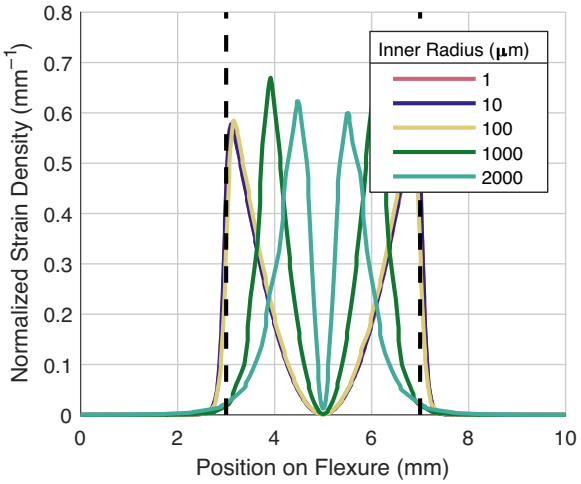

FIG. 11. The normalized distribution of the strain energy density for a cross section across the flexures at positions along the flexure length. The energy is normalized such that it is a ratio of the total energy. This is shown for different inner radii of curvatures at the flexure ends. The black dashed lines show the ends of the flexure region and the return to the bulk material. The geometry studied is the same as defined in Fig. 4.

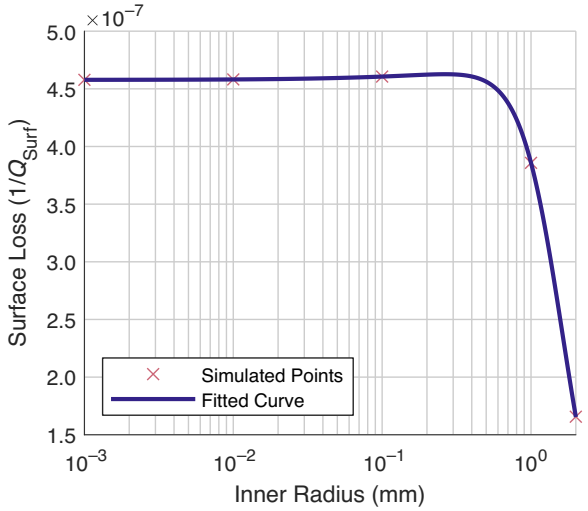

FIG. 12. The surface loss of a resonator with the geometry used in Fig. 4 when different inner radii are used. The simulation was done for the five inner radii in Fig. 11, and fitted with a cubic interpolation routine. A larger inner radius leads to a lower surface loss.

a result of stress from both ends of the flexure being pushed into the center of the flexure. Therefore, the inner radius on the height should be designed just slightly short of the flexure length when manufacturing methods allow.

The other effect that must be considered with inner radii is the effect on surface loss. Since the material loss depends on the surface-to-volume ratio, adding more material to the flexures in high-energy density regions makes sense, allowing better energy distribution along the flexure. The width can be altered by adding an inner radius to the flexure corner. A test was performed whereby different inner radii were tested to find an optimum point for the strain distribution. The inner radius was added as indicated by Fig. 2. Using a combination of static and eigenfrequency models, COMSOL was used to simulate these effects. The effect of different inner radii on the strain distribution is shown in Fig. 11. Adding the inner radius pushes the peak of the strain distribution inwards before decaying into the bulk.

The effect of this on surface loss is then shown in Fig. 12. Equation (6) was used to calculate the surface loss, with the distribution of strain densities shown in Fig. 11 as the estimate for $\epsilon(\vec{r})$ from Eq. (6). The result $d_s = 10$ μm is taken from Sec. II A 2 and a surface loss value of 1×10^{-5} from Ref. [32]. Figure 12 shows that a large inner radius leads to a lower surface loss. However, this only has a noticeable effect when the inner radii are above 10% of the flexure length. The corresponding study on extra stress in Fig. 10 shows that stress becomes more localized and requires longer compensating flexures. The extra stress scales roughly as power 1/2, while the gain in surface loss scales roughly linearly. Considering the two cases discussed in Sec. IV A, we see that the gains of surface loss are canceled out for the case in which f_0 is a free parameter above the optimum for any radius of curvature above its optimum stress point, Instead, if f_0 is fixed by external constraints, inner radii scale as power 1/4 with thermal noise. This is only true when surface losses are dominating. As the gains from increasing the inner radius are small, they should only be done when it does not add to manufacturing complexity.

When f_0 can be chosen, add an inner radius 10% of the flexure length. Alternatively, when a specific f_0 is required, the optimum radius of curvature is a little under half the length, but we only see gains while the surface loss is limited.

APPENDIX B: TOLERANCES AND MISMATCHES

The current discussion has so far focused on idealized cases. Once parts are manufactured, every defined parameter will have some deviation from the idealized case. The effect of these tolerances and how best to define them is discussed in this appendix. As the flexure region defines the resonator behavior, and minor deformities significantly impact performance, tolerances on the flexures are the most important for resonator design.

The surface profiles of flexures produced using the methods discussed in this thesis are presented in Sec. II A 2. The surface roughness is a measure of the very high spatial frequency effects. As such, its effects on the large-scale flexure geometry are limited and so only matter with regard to material loss calculations. The waviness profiles

measured in this appendix are orders of magnitude lower than the quoted geometric deviations. The tolerances of concern are those that disturb the larger flexure geometry, especially in an uneven manner.

For this study, we confine ourselves to low spatial frequency deviations from a specified flexure geometry. This would still be an infinite possibility space, but when consulting with companies and manufacturers, three typical deformations come to light that must be defined. Controlling the average width of the flexures across the structure is very difficult, with tolerances typically of the order of $\pm 10\%$. It is also possible that the flexure width of one or both flexures varies along the length of the flexure. For example, if the wafer or etching machine is not perfectly flat, the width would change linearly over its length, creating a trapezoid geometry. The trapezoid geometry affects either or both flexures and could happen in the same direction or opposite to each other. Finally, the surfaces of the test mass and base facing each other may not be flush. As the distance between the two would vary, one flexure would have to be longer to compensate for this. We investigate the impact of each of these on the design throughout this appendix.

After defining the parameters we wish to explore, we can study this again for the case of a linear resonator to understand the general effect of these mismatches. Similar studies would be needed on specific geometries that are to be manufactured. For example, we use the same linear resonator model from Fig. 4 and the same FEA model.

The effect of varying the average flexure width on the modes is shown in Fig. 13. Here, two cases are studied: one where the average width is split evenly between the two flexures and one where one flexure is held at 140-μm width and the other varied. We see limited effects on any mode from the distribution, but the mode frequency depends on the total flexure mass. The only relevant mode frequency effect is if the device can survive operation with any flexure width within quoted manufacturing tolerances. This is best done by repeating FEA simulations with extrema of the tolerances and checking safety factors in these cases.

Although the mode frequency effect was minimal in this case, the mode shape itself could be distorted. Imbalances between the flexures could lead to mode shape distortion. In practice, this distortion would mean the test mass no longer being perpendicular to the mode of oscillation. The effects of differing imbalance on the test mass angle θ, relative to the load applied, were studied using the same linear resonator as the study in Fig. 4 and the results are shown in Fig. 14. These graphs show how θ evolves with mismatches between different parameters.

Figure 14(a) shows how, under 1-g load, θ varies with the changing width of one of two flexures. The simulation shows the expected result: when the flexures are the same width, there is no angular offset, but the angle increases as the flexures mismatch changes. The test mass angle θ

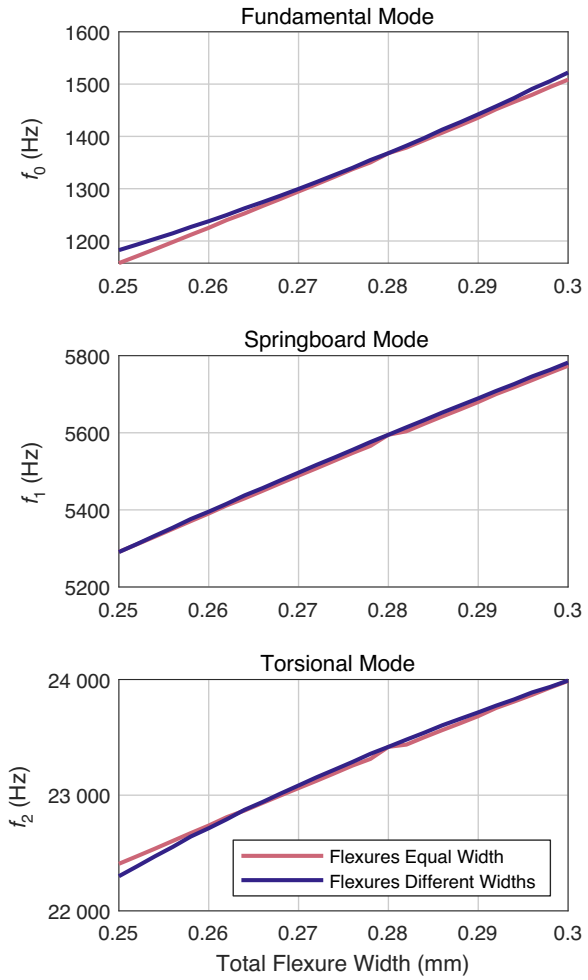

FIG. 13. Dependency of the frequencies of the first three modes of a linear resonator, with parameters described in Fig. 4, with respect to flexure width mismatches. The graph shows two cases. The red curve describes when the total flexure width is evenly divided between the two flexures. On the other hand, the blue curve is when one flexure of the pair is fixed at 0.14 mm thick while the other changes width. By comparing both, we see that the mode frequency is only slightly dependent on the ratio between the two flexures and is mostly dependent on the total width of the combined flexures.

scales linearly with respect to the load, as shown in the fourth plot in this figure. This is problematic as it is a noise source that scales with the signal, making it challenging to model. The angle of the test mass will couple into readout measurement noise through tilt-to-length coupling (TTL). The effects of TTL are subtle and numerous. They are thoroughly detailed by Hartig *et al.* [37]. The coupling to noise will vary enormously depending on the detector configuration and the readout scheme. With estimates of the angular noise introduced by the mismatch, the effect on the readout can be predicted using the models in the paper.

The effect of trapezoid-shaped flexures is shown in Fig. 14(b). Two cases are shown here, with opposite ends

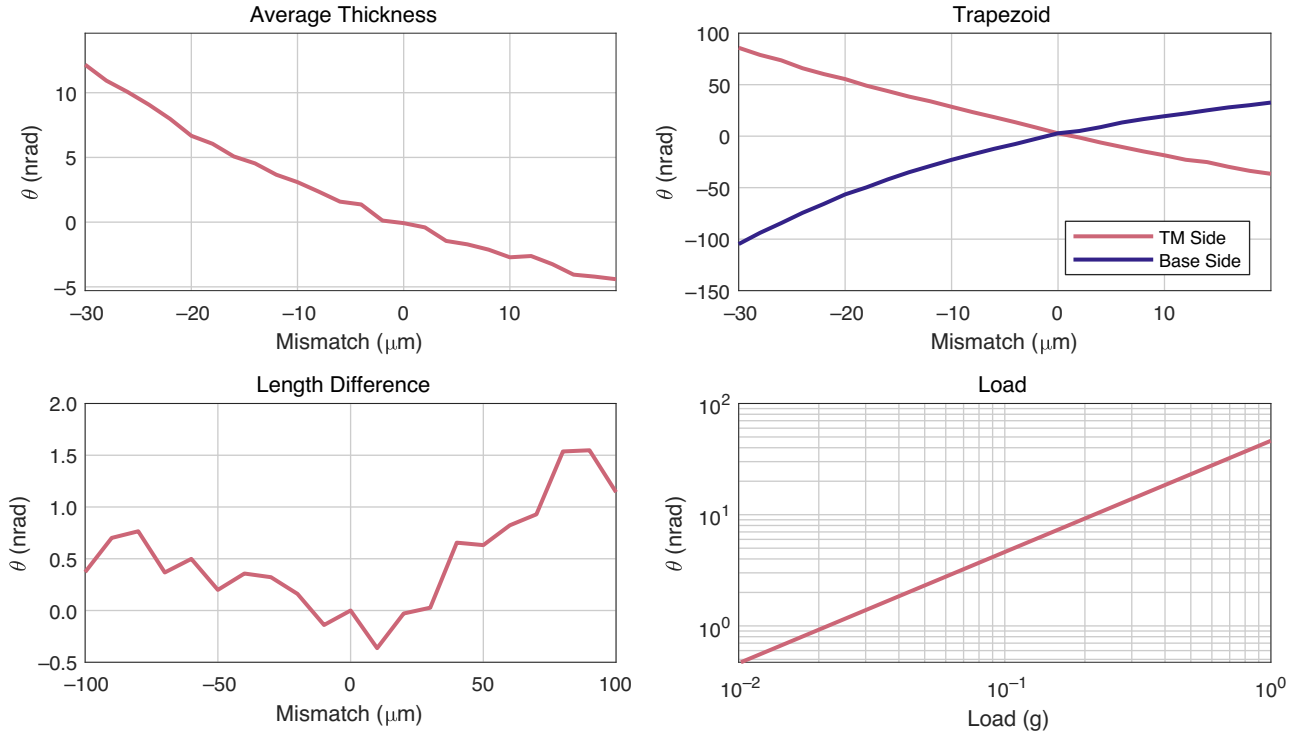

FIG. 14. The angular dependence of a linear resonator with regards to a variety of tolerance mismatches between flexure pairs. The tests were conducted with a linear resonator, as described in Fig. 4. A stationary FEA analysis was performed in COMSOL. The tests were done with 1 g of load on the resonator in the direction of the fundamental mode. The angle of the test mass relative to the load is shown for several cases. The first plot shows the case of two flexures, perfect cuboids with a width difference. The second graph shows when the flexure is a trapezoid, with the width changing over its length. The case where the base side has the correct width and the test mass side is mismatched is shown in red, while the blue line shows the opposite orientation. The length difference shows the case of one flexure being longer or shorter than the other. The fourth plot shows how a fixed mismatch with an average flexure width of 20 μm scales with θ with differing loads.

of the flexures being those that are mismatched. Both sides show similar results, but with the rotation in opposite directions. When the base is varied, a slightly greater coupling to the angle is seen, but both show a greater susceptibility to tilt than the purely average width change or length change cases. Tolerances should, therefore, be defined to minimize this criterion best. This is best done by defining a maximum and minimum value of the flexure width that cannot be exceeded at any point along the length. Typically, this criterion has an achievable ±10-μm tolerance with the methods discussed by Bellouard *et al.* [12].

The length of the two flexures was changed so that one was longer than the other. The result on θ is shown in Fig. 14(c). The effect of the length change was so small that uncertainties from the mesh elements seemed to dominate the test. Even with different lengths, each flexure can act independently and linearly without changing the mode shapes. Hence, this does not seem to be a critical criterion.

As the scale of this tilt coupling depends on load, as shown in Fig. 14(d), the relevance of this on the design will depend on environmental conditions.

[1] F. Guzman., L. Kumanchik, J. Pratt, and J. M. Taylor, High sensitivity optomechanical reference accelerometer over 10 kHz, Appl. Phys. Lett. **104**, 221111 (2014).

[2] O. Gerberding, F. Guzman., J. Melcher, J. R. Pratt, and J. M. Taylor, Optomechanical reference accelerometer, Metrologia **52**, 654 (2015).

[3] J. Carter, S. M. Kohlenbeck, P. Birckigt, R. Eberhardt, G. Heinzel, and O. Gerberding, in *2020 IEEE International Symposium on Inertial Sensors and Systems (INERTIAL)* (IEEE, Hiroshima Japan, 2020).

[4] A. Hines, L. Richardson, H. Wisniewski, and F. Guzman, Optomechanical inertial sensors, Appl. Opt. **59**, G167 (2020).

[5] A. M. H. Nelson and F. Guzman, in *Optical and Quantum Sensing and Precision Metrology II*, edited by S. M. Shahriar, J. Scheuer (SPIE, 2022).

[6] L. Kumanchik, M. Rezinkina, and C. Braxmaier, Choice of the miniature inertial optomechanical sensor geometric parameters with the help of their mechanical characteristics modelling, Micromachines **14**, 1865 (2023).

[7] L. A. Capistran, A. Hines, J. Carter, X. Guo, G. Valdes, J. Sanjuan, and F. Guzman, in *Quantum Sensing,*

Imaging, and Precision Metrology, edited by S. M. Shahriar, J. Scheuer (SPIE, San Francisco, 2023).

[8] A. Hines, A. Nelson, Y. Zhang, G. Valdes, J. Sanjuan, and F. Guzman, Compact optomechanical accelerometers for use in gravitational wave detectors, Appl. Phys. Lett. **122**, 094101 (2023).

[9] L. L. Richardson, A. Rajagopalan, H. Albers, C. Meiners, D. Nath, C. Schubert, D. Tell, E. Wodey, S. Abend, M. Gersemann, *et al.*, Optomechanical resonator-enhanced atom interferometry, Commun. Phys. **3**, 1 (2020).

[10] F. Matichard, *et al.*, Seismic isolation of advanced LIGO: Review of strategy, instrumentation and performance, Classical Quantum Gravity **32**, 185003 (2015).

[11] J. Sanjuan, X. Guo, A. Hines, A. Nelson, G. Valdes, P. Wang, and F. Guzman, in *Optica Advanced Photonics Congress 2022* (Optica Publishing Group, Maastricht, Netherlands, 2022).

[12] Y. Bellouard, A. Champion, M. Gevincevicius, C. Corbari, M. Beresna, P. Kazansky, O. Chappuis, M. Kral, R. Clavel, J. M. Breguet, *et al.*, in *Conference on Lasers and Electro-Optics 2012* (OSA, San Jose, California, 2012).

[13] R. Kirchhoff, C. M. Mow-Lowry, V. B. Adya, G. Bergmann, S. Cooper, M. M. Hanke, P. Koch, S. M. Köhlenbeck, J. Lehmann, P. Oppermann, *et al.* Huddle test measurement of a near Johnson noise limited geophone, Rev. Sci. Instrum. **88**, 115008 (2017).

[14] S. J. Cooper, C. J. Collins, A. C. Green, D. Hoyland, C. C. Speake, A. Freise, and C. M. Mow-Lowry, A compact, large-range interferometer for precision measurement and inertial sensing, Classical Quantum Gravity **35**, 095007 (2018).

[15] F. Zhou, Y. Bao, R. Madugani, D. A. Long, J. J. Gorman, and T. W. LeBrun, Broadband thermomechanically limited sensing with an optomechanical accelerometer, Optica **8**, 350 (2021).

[16] A. G. Krause, M. Winger, T. D. Blasius, Q. Lin, and O. Painter, A high-resolution microchip optomechanical accelerometer, Nat. Photonics **6**, 768 (2012).

[17] O. Gerberding, Deep frequency modulation interferometry, Opt. Express **23**, 14753 (2015).

[18] K. S. Isleif, G. Heinzel, M. Mehmet, and O. Gerberding, Compact multifringe interferometry with subpicometer precision, Phys. Rev. Appl. **12**, 034025 (2019).

[19] J. Smetana, R. Walters, S. Bauchinger, A. S. Ubhi, S. Cooper, D. Hoyland, R. Abbott, C. Baune, P. Fritchel, O. Gerberding, *et al.*, Compact Michelson interferometers with subpicometer sensitivity, Phys. Rev. Appl. **18**, 034040 (2022).

[20] Y. Yang, K. Yamamoto, V. Huarcaya, C. Vorndamme, D. Penkert, G. F. Barranco, T. S. Schwarze, M. Mehmet, J. J. E. Delgado, J. Jia, *et al.* Single-element dual-interferometer for precision inertial sensing, Sensors **20**, 4986 (2020).

[21] D. T. Smith, J. R. Pratt, and L. P. Howard, A fiber-optic interferometer with subpicometer resolution for dc and low-frequency displacement measurement, Rev. Sci. Instrum. **80**, 035105 (2009).

[22] Y. Zhang and F. Guzman, Fiber-based two-wavelength heterodyne laser interferometer, Opt. Express **30**, 37993 (2022).

[23] P. R. Saulson, *Fundamentals of Interferometric Gravitational Wave Detectors* (World Scientific, Singapore, 1994).

[24] K. Agatsuma, *Study of Pendulum Thermal Noise in Gravitational Wave Detectors* (Department of Physics, Faculty of Science, University of Tokyo, Tokyo, 2010).

[25] G. González, Suspensions thermal noise in the LIGO gravitational wave detector, Classical Quantum Gravity **17**, 4409 (2000).

[26] C. M. Zener and S. Siegel, Elasticity and anelasticity of metals, J. Phys. Colloid Chem. **53**, 1468 (1949).

[27] R. Lifshitz and M. L. Roukes, Thermoelastic damping in micro-and nanomechanical systems, Phys. Rev. B **61**, 5600 (2000).

[28] A. N. Norris and D. M. Photiadis, Thermoelastic relaxation in elastic structures, with applications to thin plates, Q. J. Mech. Appl. Math. **58**, 143 (2005).

[29] P. Chadwick, Thermal damping of a vibrating elastic body, Mathematika **9**, 38 (1962).

[30] A. Duwel, R. N. Candler, T. W. Kenny, and M. Varghese, Engineering MEMS resonators with low thermoelastic damping, J. Microelectromech. Syst. **15**, 1437 (2006).

[31] X. Guo, Y. B. Yi, and S. Pourkamali, A finite element analysis of thermoelastic damping in vented MEMS beam resonators, Int. J. Mech. Sci. **74**, 73 (2013).

[32] A. M. Gretarsson and G. M. Harry, Dissipation of mechanical energy in fused silica fibers, Rev. Sci. Instrum. **70**, 4081 (1999).

[33] K. Numata, S. Otsuka, M. Ando, and K. Tsubono, Intrinsic losses in various kinds of fused silica, Classical Quantum Gravity **19**, 1697 (2002).

[34] G. Vajente, M. Fazio, Y. Le, A. Gupta, A. Ananyeva, G. Billinsley, and S. Carmen, Method for the experimental measurement of bulk and shear loss angles in amorphous thin films, Phys. Rev. D **101**, 042004 (2020).

[35] J. J. Carter, P. Birckigt, O. Gerberding, Q. Li, R. Struening, T. Ullsperger, and S. M. Kohlenbeck, An experiment to test the mechanical losses of different bonding techniques in fused silica, arXiv:220109909.

[36] R. Nawrodt, C. Schwarz, S. Kroker, I. W. Martin, F. Brückner, L. Cunningham, V. Große, A. Grib, D. Heinert, J. Hough, *et al.*, Investigation of mechanical losses of thin silicon flexures at low temperatures, Classical Quantum Gravity **30**, 115008 (2013).

[37] M. S. Hartig, S. Schuster, and G. Wanner, Geometric tilt-to-length coupling in precision interferometry: Mechanisms and analytical descriptions, J. Opt. **24**, 065601 (2022).

[38] I. Elishakoff, *Handbook on Timoshenko-Ehrenfest Beam and Uflyand-Mindlin Plate Theories* (World Scientific, Singapore, 2020).

[39] F. Matichard, B. Lantz, K. Mason, R. Mittleman, B. Abbott, S. Abbott, E. Allwine, S. Barnum, J. Birch, S. Biscans, *et al.*, Advanced LIGO two-stage twelve-axis vibration isolation and positioning platform. Part 1: Design and production overview, Precis. Eng. **40**, 273 (2015).

[40] F. Matichard, B. Lantz, K. Mason, R. Mittleman, B. Abbott, S. Abbott, E. Allwine, S. Barnum, J. Birch, S. Biscans, *et al.* Advanced LIGO two-stage twelve-axis vibration isolation and positioning platform. Part 2: Experimental investigation and tests results, Precis. Eng. **40**, 287 (2015).

[41] J. Carter, S. Kohlenbeck, P. Birckigt, R. Eberhardt, G. Heinzel, and O. Gerberding, High precision inertial sensors on a one inch diameter optic, arXiv:2403.12632.